Lim *et al. Energy Mater.* **2025**, *5*, 500104
DOI: 10.20517/energymater.2025.08

Energy Materials

Article

Open Access

Check for updates

Partially graphitic structure-assisted hard carbon derived from lignin for sodium-ion battery anodes

Mu-Seong Lim[1], Geon Hae Lim[1], Yoon-Jung Shin[2], Ji Su Chae[1], Jae-Won Lee[2,3,*], Kwang Chul Roh[1,*]

[1]Energy Storage Materials Center, Korea Institute of Ceramic Engineering & Technology, Gyeongsangnam-do 52851, Republic of Korea.
[2]Department of Wood Science and Engineering, College of Agriculture and Life Sciences, Chonnam National University, Gwangju 61186, Republic of Korea.
[3]Interdisciplinary Program in IT-Bio Convergence System, Chonnam National University, Gwangju 61186, Republic of Korea.

***Correspondence to:** Prof. Jae-Won Lee, Department of Wood Science and Engineering, College of Agriculture and Life Sciences, Chonnam National University, 77 Yongbong-ro, Buk-gu, Gwangju 61186, Republic of Korea. E-mail: ljw43376@cheonnam.ac.kr; Dr. Kwang Chul Roh, Energy Storage Materials Center, Korea Institute of Ceramic Engineering & Technology, 101 Sohoro, Jinju-si, Gyeongsangnam-do 52851, Republic of Korea. E-mail: rkc@kicet.re.kr

How to cite this article: Lim, M. S.; Lim, G. H.; Shin, Y. J.; Chae, J. S.; Lee, J. W.; Roh, K. C. Partially graphitic structure-assisted hard carbon derived from lignin for sodium-ion battery anodes. *Energy Mater.* **2025**, *5*, 500104. https://dx.doi.org/10.20517/energymater.2025.08

Received: 13 Jan 2025 **First Decision:** 19 Mar 2025 **Revised:** 31 Mar 2025 **Accepted:** 7 Apr 2025 **Published:** 16 May 2025

Academic Editor: Jiazhao Wang **Copy Editor:** Fangling Lan **Production Editor:** Fangling Lan

Abstract

The increasing demand for efficient energy storage has led to increased research on sodium-ion batteries (SIBs) as a promising alternative to lithium-ion batteries. However, the anode materials currently employed in lithium-ion batteries are not suitable for SIBs, highlighting the need for the development of appropriate anode materials. In this study, cellulose- and lignin-rich residues extracted from wood biomass were converted to hard carbon, and their performance as anode materials for SIBs was evaluated. Cellulose and lignin were separated from larch wood using a deep eutectic solvent, followed by carbonization to produce CF-1300C and LF-1300C, respectively. Lignin undergoes partial graphitization at elevated temperatures, enhancing its electrical conductivity and forming ion insertion and extraction pathways. LF-1300C demonstrated higher crystallinity than CF-1300C owing to this graphitization and featured an interlayer spacing of approximately 0.43 nm, which facilitates sodium-ion insertion. Consequently, LF-1300C achieved a higher initial discharge capacity and Coulombic efficiency (350 mAh g^{-1} and 74%, respectively) than CF-1300C (331 mAh g^{-1} and 71%, respectively). Furthermore, LF-1300C exhibited a 21% and 84% improvement in rate capability and cycle retention, as compared with CF-1300C. These results indicate that hard carbon with a partially graphitized structure exhibits significant potential for use as an anode material in SIBs, especially in cases where existing crystalline materials present challenges. This study highlights the

advantages of lignin-derived hard carbon as a superior anode material for SIBs, providing an eco-friendly and scalable solution for energy storage.

Keywords: Hard carbon, sodium-ion batteries, biomass, cellulose, lignin

INTRODUCTION

The increasing demand for electric vehicles and energy-storage systems has highlighted the need for high-performance energy-storage devices. Lithium-ion batteries (LIBs) are currently the most widely used energy-storage technology owing to their excellent performance. However, LIBs exhibit several challenges, including the limited availability and geographical concentration of lithium and the significant environmental impacts associated with its extraction and processing[1,2]. These issues have prompted research into alternative energy-storage technologies. Consequently, sodium (Na)-ion batteries (SIBs) have emerged as promising alternatives, enabling the utilization of the abundant Na resources available on Earth for energy storage[3,4]. SIBs exhibit a charge/discharge mechanism similar to that of LIBs, offering a familiar operational framework[5]. Notably, the inert nature of Na toward Al allows its use as a cost-effective current collector, replacing the more expensive Cu typically used in LIBs[6,7]. These advantages enhance the appeal of SIBs, positioning them as a compelling option for evolving energy-storage devices.

Despite these advantages, SIB technology has not yet reached maturity and current research is largely focused on the selection and optimization of anode materials. Carbon (C)-based anode materials can be categorized into two primary types, namely, graphitizable carbon such as graphite, graphene, and carbon nanotubes (CNTs), and non-graphitizable carbon, including soft and hard carbon[8]. Graphite is preferred for commercial LIBs because of its high volumetric capacity and excellent cycling performance. However, its use as an anode material for SIBs presents challenges[9]. The larger atomic mass, higher volume, and larger ionic radius of Na ions than those of Li ions complicate the intercalation and deintercalation processes within the graphite layers (~0.34 nm)[8-11]. Consequently, carbon materials without sufficient interlayer spacing are considered unsuitable for SIBs. To address these issues, expanded graphite with enhanced interlayer spacing has been proposed as an anode material for SIBs[8,12,13]. Although graphitizable carbon materials, such as graphene and CNTs, exhibit promising characteristics for Na-ion storage owing to their large surface areas and surface defects, their manufacturing processes are typically complex and costly when used as standalone materials[10,14,15].

Consequently, non-graphitizable carbon has emerged as a viable and advantageous option for SIB anodes[8,15]. Non-graphitizable carbon materials can effectively accommodate Na ions because of their diverse structural defects and irregular arrangements, and their production processes are relatively straightforward and cost-effective. Among the non-graphitizable carbon materials, soft carbon exhibits a low initial Coulombic efficiency (ICE) owing to its high defect density[8]. In contrast, hard carbon, which possesses a wider interlayer spacing (0.37-0.42 nm) and lower operating potential, is a suitable candidate for SIB anodes[15,16]. The intrinsic pores and expanded interlayer spacing in hard carbon effectively promote the storage and diffusion of Na ions and the abundant edges and defects provide numerous sites for efficient Na-ion storage[16]. In contrast to typical precursors, hard carbon is primarily produced through the pyrolysis of biomass, with previous studies successfully demonstrating the feasibility of deriving hard carbon from various biomass sources such as coconut shells[17], walnut shells[17], and corncob[18].

Biomass sources primarily include hemicellulose, cellulose, and lignin. Although cellulose and hemicellulose are widely used in the production of paper, pharmaceuticals, and bioethanol, the complex molecular structure of lignin limits its commercial viability[19,20]. Only approximately 2% of globally produced lignin is

utilized commercially, with the majority being treated as low-value waste[20]. However, the polymeric structure and high carbon content of lignin render it a promising precursor for various carbon materials[20-22]. Previous studies reported that the partial crystallinity induced at elevated temperatures can increase the electrical conductivity of electrode materials[19]. The sufficient interlayer spacing for the deintercalation of Na ions and enhanced electrical conductivity, which is facilitated by the partial crystallinity, could render lignin-based hard carbon an effective anode material for SIBs. However, lignin-derived partially crystalline hard carbon has not been reported as an anode material for SIBs.

Wood biomass was fractioned in this study into cellulose-rich (CF) and lignin-rich fractions (LF) using a deep eutectic solvent (DES), and each fraction was converted to hard carbon for use as an anode material for SIBs. CF and LF were carbonized at 1,300 °C to produce hard carbon and their physical properties were analyzed and compared. The resulting hard carbon materials were applied as anode materials in SIBs and their electrochemical performances were evaluated.

EXPERIMENTAL

Biomass and carbonization

Larch (*Larix kaempferi*) biomass was pretreated using a DES to obtain CF and LF. The DES used in this study was synthesized by mixing choline chloride and lactic acid in a weight ratio of 1:10. It was synthesized by mixing choline chloride and lactic acid in a weight ratio of 1:10. The DES solution (200 g) was combined with 5 g biomass and pretreated in an oil bath at 130 °C for 9 h. The pretreated biomass was then separated into solid and liquid phases through filtration. The solid CF was sequentially washed with acetone and distilled water, and subsequently dried at 45 °C. The liquid LF was diluted ten-fold with distilled water and allowed to stand for 12 h. The diluted liquid fraction was then centrifuged at 4,000 rpm and 4 °C, and the resulting precipitate was collected. The precipitate was further washed with 10% ethanol to eliminate any residual DES and subsequently freeze-dried. Prior to carbonization, all samples were dried at 120 °C for 24 h to remove moisture. After drying, 30 g of the dried samples were carbonized at 1,300 °C for 2 h under a N_2 atmosphere in a horizontal furnace.

Characterization of materials

The biomass composition was determined using the National Renewable Energy Laboratory method. The ash content was determined using the Technical Association of the Pulp and Paper Industry T211 om-02 method at a temperature of 775 ± 25 °C over a 6-h period. Inductively coupled plasma mass spectrometry (ICP-MS) using a Nexion 300X instrument (PerkinElmer, Waltham, MA, USA) was employed to quantify the inorganic components in the biomass. The chemical composition and structure of LF and CF were analyzed using Attenuated total reflectance-Fourier transform infrared (ATR-FTIR) spectroscopy (Spectrum 400, PerkinElmer Ltd., Buckinghamshire, UK). The analysis was conducted with a spectral resolution of 4 cm^{-1}, a scanning range of 4,000-500 cm^{-1}, and four scans per minute. The elements were identified using X-ray photoelectron spectroscopy (XPS, PHI 5000 VersaProbe, ULVAC-PHI Inc., Osaka, Japan). Sugars and degradation products in the hydrolysate were analyzed using high-performance liquid chromatography (HPLC, Waters e2695, Alliance, USA) equipped with an Aminex HPX-87H column (300 × 7.8 mm^2, Bio-Rad, USA) and a refractive index detector (Waters 2414 System, USA). The analysis was performed with a 5 mM sulfuric acid solution as the mobile phase at a flow rate of 0.6 mL/min for 55 min. Thermogravimetric analysis (TGA; NETZSCH, Germany) was conducted in an air atmosphere from 25 to 1,000 °C at a heating rate of 5 °C/min. Field-emission scanning electron microscopy (FE-SEM; JSM-6700F, JEOL, Japan) was used to examine the structural morphology of the samples. High-resolution transmission electron microscopy (HR-TEM; JEM-2200FS, JEOL, Japan) was utilized to obtain TEM images and high-angle annular dark-field images. X-ray diffraction (XRD; Rigaku D/Max 2500/PC, Japan) analyses were conducted using Cu Kα radiation (λ = 0.154 nm) at 40 kV and 200 mA. Cross-sectional images of the

electrodes were obtained using focused ion beam scanning electron microscopy (FIB-SEM; Helios G4 UC, Thermo Fisher Scientific, USA). Raman spectroscopy (LabRAM HR, HORIBA Jobin Yvon SAS, Japan) was performed using an Ar-ion laser.

Electrochemical measurements

The anodes were fabricated at room temperature and subsequently dried in a vacuum oven at 80 °C for 10 h. After drying, Half-cell tests were conducted using CR2032 coin cells, which were assembled in a dry room under controlled conditions. Anodes were prepared using a slurry consisting of 80 wt.% active material, 10 wt.% Super P (TIMCAL Graphite & Carbon Co., Belgium), and 10 wt.% poly(acrylic acid) (PAA, 2 wt.% solution in distilled water; Sigma-Aldrich). PAA was selected over the commonly used a poly(vinylidene fluoride) (PVDF) binder due to its superior adhesion, ability to accommodate volume changes, and enhanced chemical stability[23]. The slurry was uniformly applied on Al foil using the doctor-blade technique, followed by drying in a vacuum oven at 80 °C for 10 h. The electrolyte solution was prepared by dissolving 1 M $NaClO_4$ in a 1:1 (v/v) mixture of ethylene carbonate (EC) and diethyl carbonate (DEC) with 5 vol% fluoroethylene carbonate (FEC) as an additive, following established protocols for SIB electrolytes[24]. The separator used was a polypropylene membrane (Celgard 2400). For evaluating Na-ion storage performance of the anodes in SIBs, half-cells were constructed, where the working electrode was a hard carbon electrode, and the counter electrode was sodium metal. Electrochemical charge-discharge cycling tests of the half-cells were conducted between 0.01 and 2.0 V *vs.* Na/Na^+ using a potentiostat/galvanostat (WPG 100, WonATech) at room temperature. Charging (sodiation) was performed at 0.2 C to 0.01 V, followed by a constant voltage step at 0.01 V until the current dropped to 0.02 C, and discharging (desodiation) was carried out at 0.2 C. The LF and CF-based hard carbon anode was prepared with a mass loading of ~0.45 mg/cm^2, ensuring accurate control of the weight of the active material. Rate performance was tested at 0.2 C, 0.5 C, 1 C, and 2 C with 5 cycles per rate, followed by long-term cycling at 0.5 C for 100 cycles to evaluate stability and capacity retention. The current densities and specific capacities were determined based on the mass of the active material. Electrochemical impedance spectroscopy (EIS) measurements were conducted using a BioLogic SAS VSP over a frequency range of 0.1 Hz to 100 kHz.

RESULTS AND DISCUSSION

Characterization of materials

Table 1 lists the chemical composition of the biomass. The raw materials (RMs) consisted of 28.09% lignin and 44.88% glucan, with galactan being the main hemicellulose component. DESs are employed to decompose lignin and hemicellulose by decomposing the ester and ether bonds in the cell walls of biomass[25]. Therefore, lignin was effectively decomposed to obtain CF, which is consistent with previously reported results[26]. The CF was primarily composed of glucan (78.71%) and contained a small amount of lignin, whereas the LF was composed of 86.12% lignin and a small amount of glucan. The ether and ester bonds were not completely decomposed during the DES pretreatment; therefore, the LF contained a small amount of glucan[25]. Figure 1 shows the crystallinity of RM, CF, and LF. RM and CF exhibit peaks at 16.4°, 22.6°, and 34.4°, which are typical peaks corresponding to the crystalline region, indicating that the biomass has a crystalline structure[26,27]. The crystallinity of CF increased from 41.34% to 60.81%, as compared with that of RM, which is attributed to the relative glucan content increase caused by the hemicellulose and lignin decomposition[26]. The DES pretreatment did not significantly alter the crystal structure. In contrast, LF exhibited a broad peak at 22.6° corresponding to the amorphous structure of lignin[28], which is consistent with the chemical composition results [Table 1].

The structural properties of each fraction were investigated using FTIR spectroscopy [Figure 2]. RM exhibits peaks corresponding to cellulose at 3,700-3,000, 1,376, 1,112, 1,061, 1,035, and 898 cm^{-1}. These peaks are related to the -OH stretching, bending vibration of the C-H group, skeletal vibration of C-OH, ester

Table 1. Chemical composition of RM, CF, and LF (unit: %)

	RM	CF	LF
Lignin	28.09 (0.18)	8.70 (0.49)	86.12 (1.43)
Glucan	44.88 (0.65)	78.71 (1.41)	3.89 (0.39)
Xylan	4.74 (0.55)	0.39 (0.55)	N.D.*
Galactan	10.94 (0.49)	N.D.*	N.D.*
Arabinan	0.24 (0.08)	0.06 (0.00)	N.D.*
Mannan	7.84 (0.15)	3.12 (0.38)	N.D.*

RM: Raw material; CF: cellulose-rich; LF: lignin-rich fractions; N.D.*: not detected.

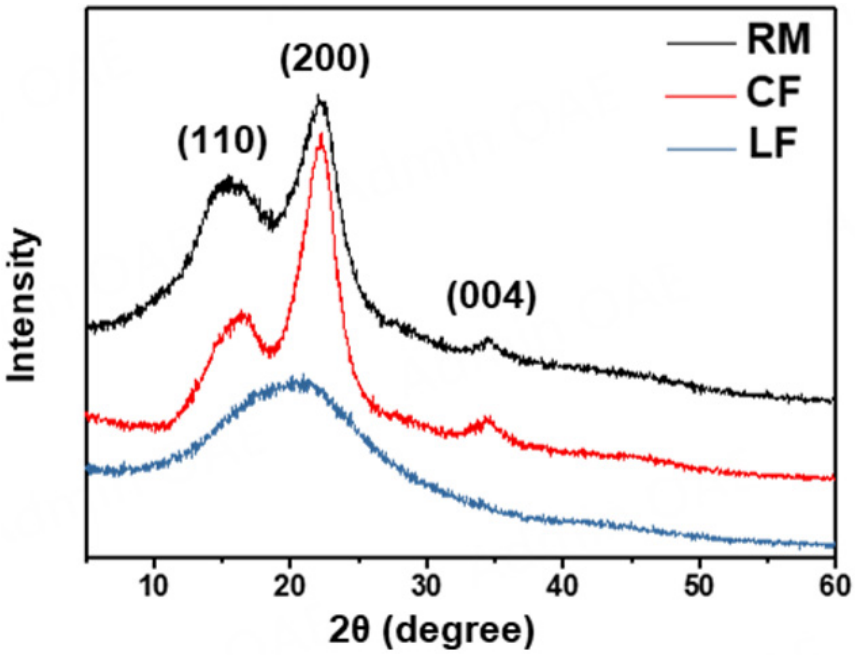

Figure 1. XRD patterns of RM, CF, and LF.

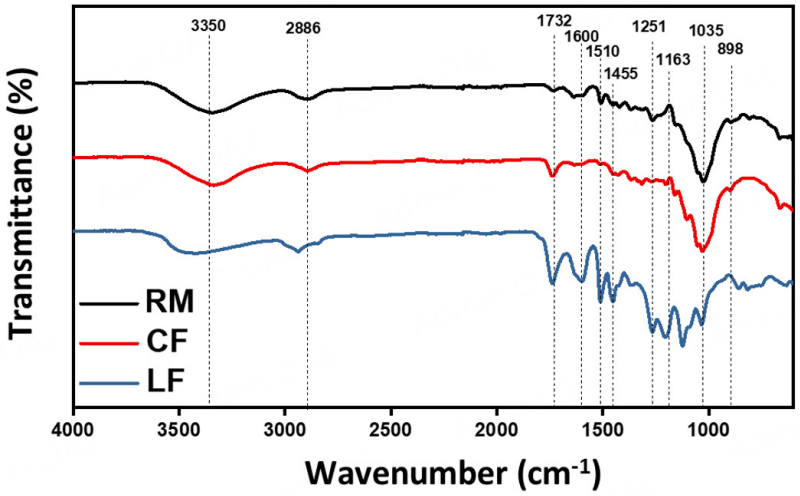

Figure 2. ATR-FTIR spectra of RM, CF, and LF.

bond of C-O-C, C-O stretching, and C-O-C stretching in the β-1,4-glycosidic linkage in cellulose, respectively[29-31]. Peaks corresponding to hemicellulose are apparent at 1,388, 1,251, 1,163, 1,080, 1,043, and 993 cm^{-1}. The peaks at 1,388, 1,043, and 1,251 cm^{-1} correspond to the C-O stretching and acetyl groups[31,32]. The peaks appearing at 1,163 and 993 cm^{-1} correspond to arabinogalactan, confirming the hemicellulose structure of the larch biomass[31]. The peaks at 1,508, 1,420, 1,225, and 1,034 cm^{-1} are related to lignin and correspond to the C=C stretching and C-H and C-O stretching of the methoxyl group[33]. The CF FTIR spectrum exhibits peaks corresponding to cellulose, similar to that of RM, with a wide peak at 1,035 cm^{-1} being clearly visible after the DES pretreatment, which is attributed to the increase in the cellulose content after the DES pretreatment [Table 1]. In contrast, the DES pretreatment reduced the intensities of the peaks corresponding to lignin and hemicellulose. The intensities of the peaks corresponding to cellulose and hemicellulose for LF decreased, whereas those corresponding to lignin increased. Peaks corresponding to the stretching vibration related to the aromatic ring skeleton of lignin are clearly visible at 1,600, 1,510, and 1,455 cm^{-1}, which indicate that lignin was well-separated and that its aromatic ring structure did not change significantly[25], which is consistent with the chemical composition results [Table 1]. Table 2 lists the elemental analysis results of RM, CF, and LF. The C content in CF was lower than that in RM because of the delignification of the biomass. The DES pretreatment reduced the lignin content and increased the cellulose ratio, which is consistent with the chemical composition analysis results [Table 1]. However, the C and O contents in LF, as compared with those in RM, increased to 62.17% and decreased to 32.28%, respectively. This was attributed to the lignin condensation reaction caused by the organic acids contained in the DES solution[34]. The O/C ratio of the CF increased to 0.86, indicating an increase in the number of O-containing functional groups[35], suggesting that the C-O bond in the lignin structure was broken[34].

The CF and LF samples carbonized at 1,300 °C were denoted as CF-1300C and LF-1300C, respectively. The surface morphology of the samples was analyzed using FE-SEM as shown in Figure 3. Figure 3A and B shows images of CF and LF before carbonization, respectively, indicating that the two samples exhibit different colors and particle sizes. Figure 3C and D shows FE-SEM images of CF and LF, respectively, before carbonization, and Figure 3E and F presents FE-SEM images of the CF and LF, respectively, after carbonization at 1,300 °C. The surface morphologies of the carbonized samples are not significantly different. The CF sample exhibits holes of a specific size, which are commonly observed in biomass. Figure 4A and B shows HR-TEM images of the two samples. CF-1300C exhibits a relatively amorphous structure compared to LF-1300C, as evidenced by the diffuse patterns observed in the fast Fourier transform (FFT). In contrast, LF-1300C exhibits a mixed partially graphitic and amorphous structure. The FFT analysis confirmed the presence of a crystalline structure with an interlayer spacing of approximately 0.43 nm. The interlayer spacing of LF-1300C is conducive to the smooth intercalation of Na ions, rendering it a suitable anode for SIBs.

In addition to HR-TEM, XRD and Raman spectroscopy were conducted to examine the graphitized structures. Figure 4C shows the XRD patterns of CF-1300C and LF-1300C, which exhibit peaks corresponding to the (002) reflection and an ordered graphitic domain reflection. These reflections originate from the inter-graphene layer stacking, whereas the (100) reflections correspond to ordered graphitic domains. The intensities of the (002) and (100) peaks of LF-1300C were higher than those of CF-1300C, suggesting that LF-1300C has a more stable crystallographic structure than amorphous-like C. These findings were substantiated by the Raman spectroscopy results, which show that CF-1300C and LF-1300C exhibit the D- and G-bands at approximately 1,350 and 1,590 cm^{-1}, respectively [Figure 4D]. The D- and G-bands are critical indicators of the structural characteristics of C materials. The D-band, observed at approximately 1,350 cm^{-1}, is attributed to structural defects, disorder, or edge effects in sp^2 carbon materials. This band is typically absent in highly crystalline graphite but becomes pronounced with the introduction of

Table 2. Elemental compositions of RM, CF, and LF

	RM	CF	LF
C (%)	48.43	44.06	62.17
H (%)	8.00	6.15	5.39
O (%)	45.98	50.28	32.28
S (%)	1.15	0.09	0.16
N (%)	1.40	0.24	0.27
H/C	1.98	1.67	1.04
O/C	0.71	0.86	0.39

RM: Raw material; CF: cellulose-rich; LF: lignin-rich fractions.

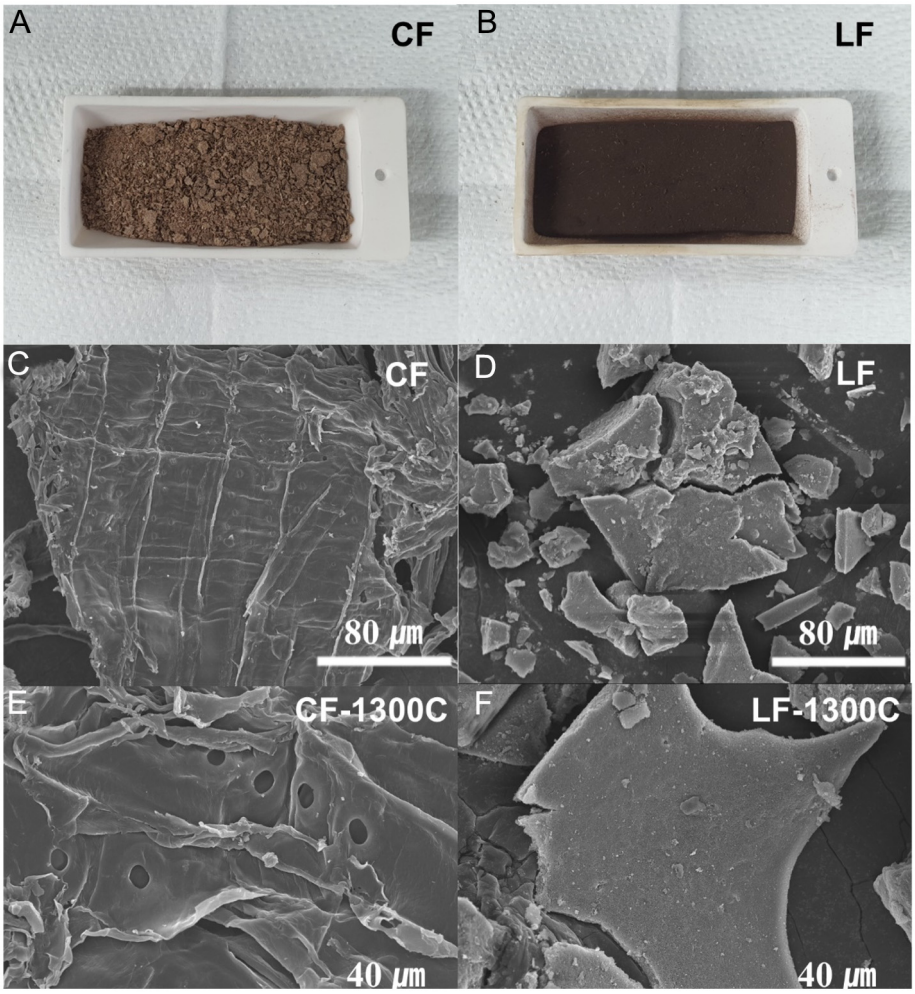

Figure 3. Photographic images of (A) CF and (B) LF. FE-SEM images of (C) CF, (D) LF, (E) CF-1300C, and (F) LF-1300C.

structural irregularities. The D-band is attributed to the A1g breathing mode of six-membered aromatic rings, which becomes active in the presence of disorder within the C lattice and serves as a valuable indicator of the defect density in the material. The G-band at approximately 1,580 cm^{-1} results from the in-plane bond-stretching motion of sp^2-bonded C atoms. The G-band corresponds to the E_{2g} vibrational mode of the graphitic lattice and serves as an indicator of the quality and integrity of the graphene planes. The

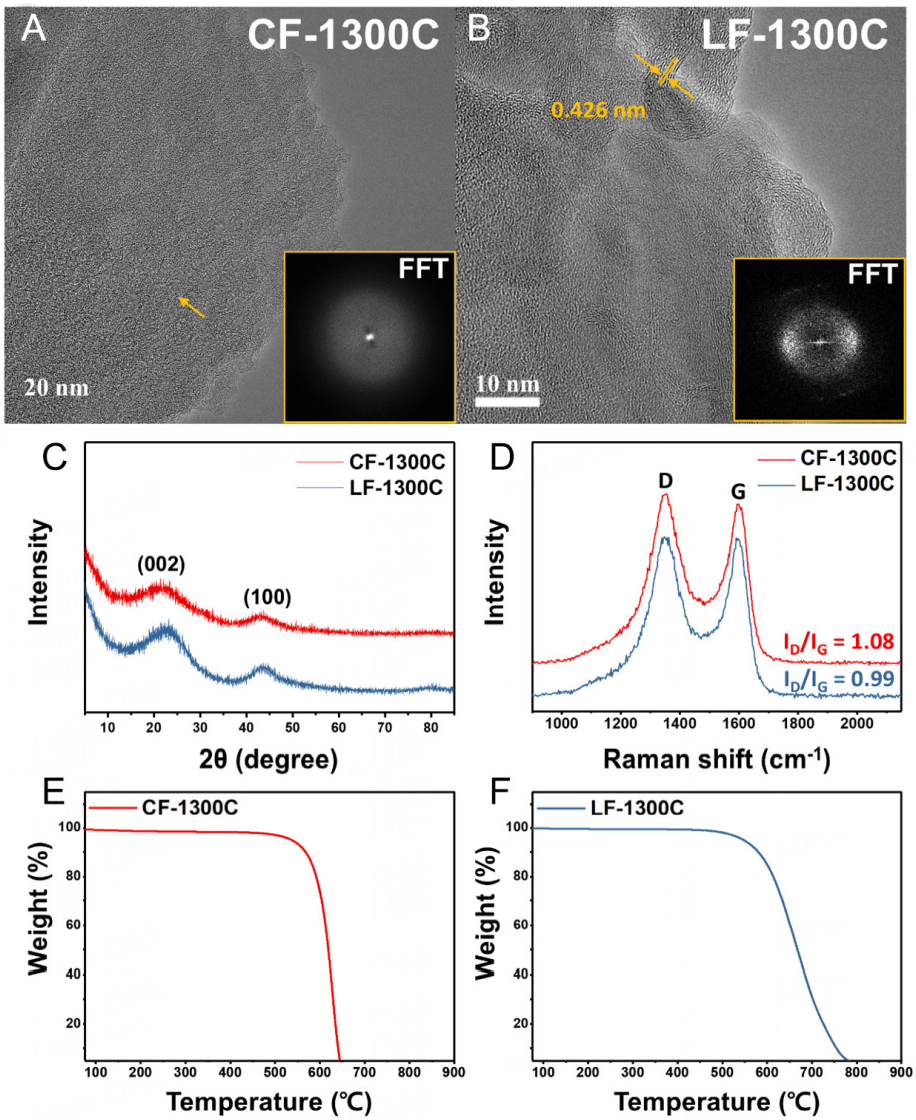

Figure 4. HR-TEM images of (A) CF-1300C and (B) LF-1300C. The inset images show the diffraction patterns obtained via FFT. (C) XRD patterns and (D) Raman spectra of CF-1300C and LF-1300C. TGA results for (E) CF-1300C and (F) LF-1300C.

I_D/I_G ratio, derived from the intensities of the G- and D-bands, serves as an indicator of defect density in carbon-based materials. For CF-1300C and LF-1300C, the I_D/I_G ratios were found to be 1.08 and 0.99, respectively. The higher I_D/I_G ratio of CF-1300C than that of LF-1300C suggests that LF-1300C exhibits a higher degree of crystallinity. All samples contained numerous sp^2 C atoms, with both samples exhibiting comparable results. Figure 4E and F show the TGA curves of CF-1300C and LF-1300C, respectively. Neither sample exhibits weight loss up to 500 °C; however, the weight significant decreases at approximately 550 °C. Carbon typically oxidizes in air at temperatures exceeding 500 °C, leading to weight loss. However, C materials with crystalline structures, such as graphite, exhibit higher oxidation temperatures[36]. Figure 4E and F indicate that LF-1300C exhibits a higher weight-loss temperature than CF-1300C, suggesting its stronger crystalline C structure.

XPS analyses were conducted to confirm the binding properties of the samples and elucidate their elemental composition and chemical state. The XPS spectra of CF-1300C and LF-1300C were subjected to optimized curve-fitting procedures within the binding energy range of 280.0-292.0 eV, as shown in Figure 5. Table 3 lists the atomic and calculated non-functional and functional C atom contents for both samples. Both samples exhibited C and O contents of > 96% and < 4%, respectively, on their surfaces. The deconvoluted C1s XPS spectra of CF-1300C and LF-1300C, presented in Figure 5, demonstrate that both samples are primarily composed of graphitic carbon (sp2), which constitutes over 68% of the total carbon species.

Electrochemical characterization of biomass

The electrochemical properties of CF-1300C and LF-1300C as SIB anode materials were thoroughly investigated [Figure 6]. While the precise mechanism of Na storage in hard carbon materials remains a subject of debate, two distinct potential regions are generally recognized, namely, a sloping region from 2.0 to 0.15 V associated with the storage of Na^+ ions in various sites within the C structure, including defects, edges, surfaces, and pores, and a plateau region below 0.1 V primarily attributed to the storage of Na^+ ions within the graphitic structures of the C materials[37].

Figure 6A and B shows typical galvanostatic charge-discharge (GCD) curves for CF-1300C and LF-1300C in the Na half-cell at a rate of 0.2 C. The initial charge/discharge capacities of CF-1300C and LF-1300C are 232/331 and 261/350 mAh g^{-1}, respectively, with corresponding ICEs of 71% and 74%. LF-1300C exhibits slightly higher ICE values and specific capacities than CF-1300C. As described in "Section Characterization of materials", LF-1300C exhibits partially graphitic structures, which results in a longer flat region below 0.1 V in the discharge graph, as compared with that of CF-1300C. This suggests that Na+ ion intercalation plays a more significant role in LF-1300C, leading to enhanced electrochemical performance.

LF-1300C also demonstrates lower irreversibility than CF-1300C, which is attributed to the lower fraction of amorphous carbon. Amorphous carbon regions tend to immobilize Na+ ions within disordered structures, contributing to irreversible capacity loss. In contrast, the partially graphitized regions in LF-1300C provide more ordered pathways for Na+ intercalation and extraction, reducing irreversible capacity loss and enhancing long-term cycling stability. Additionally, the balance between graphitic domains and amorphous regions in LF-1300C plays a crucial role in achieving stable electrochemical performance.

The rate capabilities of CF-1300C and LF-1300C were evaluated through GCD tests at various current densities ranging from 0.2 to 2 C. Following these tests, a recovery cycle at 0.5 C was performed to assess capacity recovery after high-rate cycling [Figure 6C]. The specific capacities of CF-1300C at current densities of 0.2, 0.5, 1, and 2 C are 246, 177, 110, and 68 mAh g^{-1}, respectively, whereas LF-1300C exhibits higher capacities of 263, 228, 182, and 127 mAh g^{-1} at the same current densities. Both samples exhibit capacity decay with increasing current density but recover close to their initial values at 0.5 C, indicating excellent structural stability.

The superior rate performance of LF-1300C is attributed to its partially graphitized structure, which enhances Na+ intercalation efficiency and electrical conductivity compared to the amorphous CF-1300C. The graphitic domains in LF-1300C facilitate faster charge transfer and improved Na+ diffusion kinetics, leading to enhanced performance under high-rate conditions. To quantify this conductivity, an EIS analysis was conducted. As shown in the Nyquist plot in Supplementary Figure 1, LF-1300C exhibits a smaller semicircle diameter in the high-frequency region, indicating lower charge-transfer resistance. These results highlight the critical role of partial crystallinity in enhancing rate performance and overall electrochemical properties.

Table 3. Atomic contents and chemical states obtained from the C1s peak fitting of CF-1300C and LF-1300C

	CF-1300C		LF-1300C	
	Atomic content (%)			
C	96.6		98.1	
O	3.4		1.9	
Surface groups	BE[a] (eV)	Content (%)	BE (eV)	Content (%)
Graphitic (sp^2)	283.8	68.5	283.7	70.0
C-C (sp^3)	284.9	7.9	284.6	11.8
C-O	285.5	6.5	285.5	5.9
C=O	286.6	5.9	286.6	4.2
O-C=O	288.4	5.6	288.3	4.3
π - π^*	290.2	5.6	290.1	3.8

[a]Binding energy.

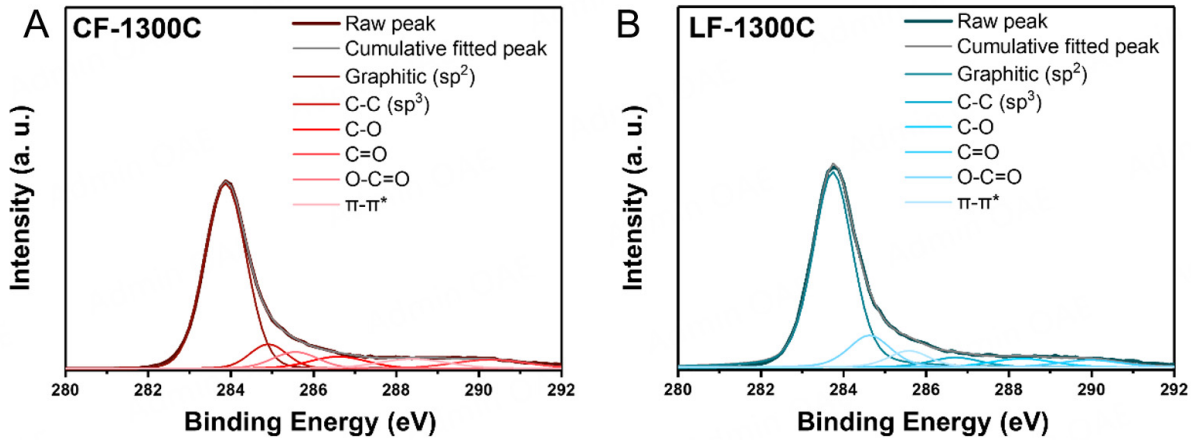

Figure 5. C1s peaks in the XPS spectra of (A) CF-1300C and (B) LF-1300C.

The capacity retention rates for CF-1300C and LF-1300C from 0.2 to 2 C were 27% and 48%, respectively. Specifically, CF-1300C and LF-1300C outperformed phenolic resin-derived hard carbon (311 mAh g^{-1}, 63% ICE) and sorghum stalk waste-derived hard carbon (259 mAh g^{-1}, 59% ICE) in initial discharge capacity and ICE, as shown in Table 4, while LF-1300C's rate capability (127 mAh g^{-1} at 2 C) and 48% retention from 0.2 C to 2 C aligned closely with high-performing waste tea-derived hard carbon (282 mAh g^{-1}, 69% ICE), as shown in Table 4[38-40]. Additionally, LF-1300C's 84% capacity retention improvement over CF-1300C after 100 cycles at 0.5 C exceeds that of polyvinyl chloride-derived hard carbon (389 mAh g^{-1}, 70% ICE) in stability[41]. Notably, LF-1300C's initial capacity and ICE are comparable to or higher than those of biomass-derived hard carbons reported in recent reviews and studies[42-44], suggesting that its partial crystallinity enhances electrical conductivity and thereby contributes to superior electrochemical performance.

CONCLUSIONS

This study evaluated and compared the changes in the physical properties of lignin- and cellulose-derived hard C, focusing on their structural differences. Moreover, the applicability of such hard carbon compounds as anode materials for SIBs was verified. LF and CF, both extracted from biomass, were employed as SIB anode materials. LF-1300C exhibited partial graphitization, resulting in higher crystallinity than that of CF-1300C. This structural characteristic enhanced the diffusion pathways for Na ions and reduced resistance, thereby increasing the specific capacitance and ICE of the SIBs. Furthermore, lignin retained or formed

Table 4. Performance of different hard carbon materials as anodes for SIBs

Electrode active material	Carbonization temperature (°C)	d-spacing (Å)	Initial discharge capacity (mAh g^{-1})	Current density (mA g^{-1})	ICE (%)	Ref.
LF-1300C	1,300	4.3	350	30	74	This work
CF-1300C	1,300	3.7	331	30	71	This work
Phenolic resin	1,500	3.7	311	20	63	[38]
Waste tea	1,400	3.9	282	30	69	[39]
Sorghum stalk waste	1,300	3.8	259	20	59	[40]
Polyvinyl chloride	700	4.0	389	12	70	[41]
Bamboo	1,300	4.1	328	30	68	[42]
Wood fiber	1,000	-	240	20	72	[43,44]

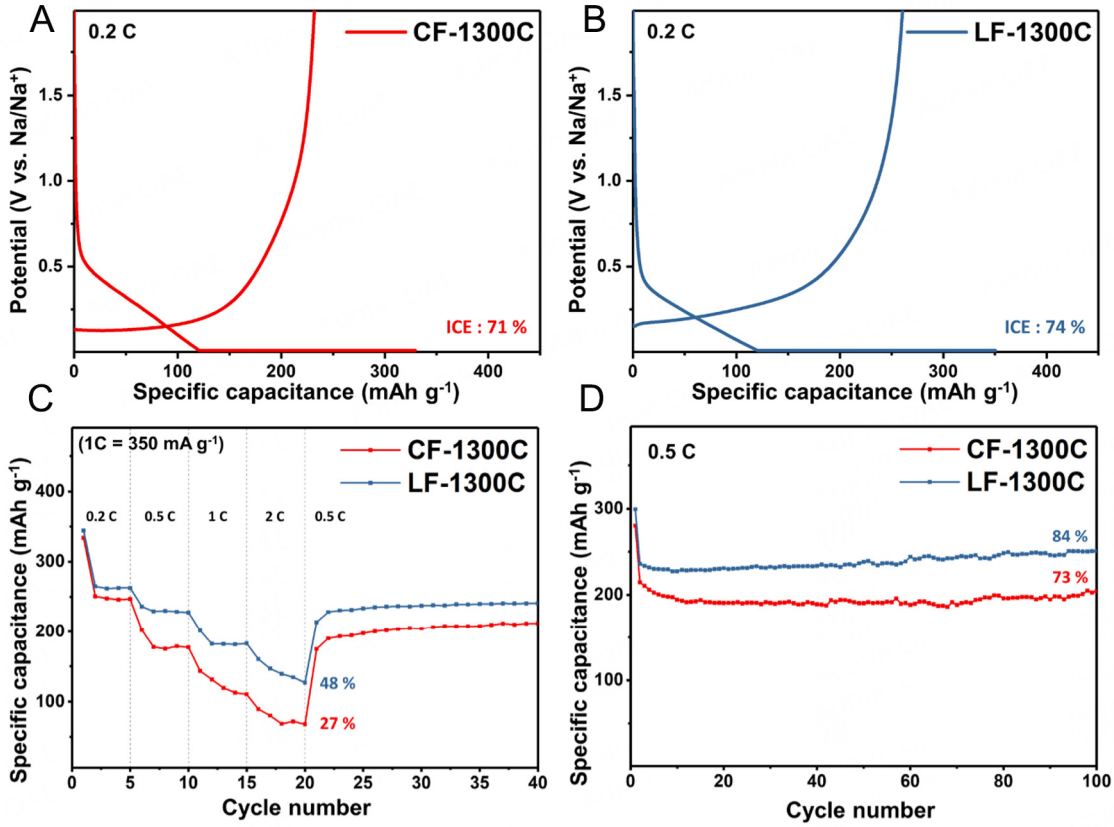

Figure 6. Electrochemical performance of CF-1300C and LF-1300C: (A and B) first GCD curve at 0.2 C in the potential window of 0.01-2.0 V, (C) rate performance at various current densities, and (D) cycling performance at 0.5 C.

layered structures through a simple process; thus, LF-1300C exhibited superior electrochemical performance to CF-1300C. These results highlight not only the economic and environmental potential of converting low-value lignin to energy-storage materials but also the scalability and viability of partially graphitized materials as anode materials in SIBs, in which the use of crystalline anode materials has historically been challenging.

DECLARATIONS

Authors' contributions

Conceptualization, data curation, validation, investigation, methodology, writing - original draft: Lim, M. S.
Data curation, validation, investigation, methodology, writing - original draft: Lim, G. H.
Resources: Shin, Y. J.
Writing - review and editing: Chae, J. S.; Lee, J. W.
Writing - review and editing, project administration, supervision: Roh, K. C.

Availability of data and materials

The data that support the findings of this study are available from the corresponding author upon reasonable request.

Financial support and sponsorship

This study was supported by the Technology Innovation Program RS-2024-00409090 (Development of High-Capacity/High-Efficiency Hard Carbon Anode Material and Mass Production Technology for High-Energy Density (160 Wh/kg) Sodium-Ion Batteries) funded by the Ministry of Trade, Industry & Energy (MOTIE, Korea) and the Technology Innovation Program RS-2024-00409900 (Development of a Polyolefin-Based Ceramic Coating Separator for Sodium-Ion Batteries) funded by the Ministry of Trade, Industry & Energy (MOTIE, Korea).

Conflicts of interest

All authors declared that there are no conflicts of interest.

Ethical approval and consent to participate

Not applicable.

Consent for publication

Not applicable.

REFERENCES

1. Costa, C.; Barbosa, J.; Gonçalves, R.; Castro, H.; Campo, F. D.; Lanceros-Méndez, S. Recycling and environmental issues of lithium-ion batteries: advances, challenges and opportunities. *Energy. Storage. Mater.* **2021**, *37*, 433-65. DOI
2. Gu, Z. Y.; Wang, X. T.; Heng, Y. L.; et al. Prospects and perspectives on advanced materials for sodium-ion batteries. *Sci. Bull.* **2023**, *68*, 2302-6. DOI
3. Zhao, L.; Zhang, T.; Li, W.; et al. Engineering of sodium-ion batteries: opportunities and challenges. *Engineering* **2023**, *24*, 172-83. DOI
4. Kubota, K.; Dahbi, M.; Hosaka, T.; Kumakura, S.; Komaba, S. Towards K-ion and Na-ion batteries as "beyond Li-ion". *Chem. Rec.* **2018**, *18*, 459-79. DOI PubMed
5. Zhou, L.; Cui, Y.; Niu, P.; et al. Biomass-derived hard carbon material for high-capacity sodium-ion battery anode through structure regulation. *Carbon* **2025**, *231*, 119733. DOI
6. Wang, K.; Wang, C.; Yang, H.; et al. Vertical graphene nanosheetsmodified Al current collectors for high-performance sodium-ion batteries. *Nano. Res.* **2020**, *13*, 1948-54. DOI
7. Zhou, H.; Song, Y.; Zhang, B.; et al. Overview of electrochemical competing process of sodium storage and metal plating in hard carbon anode of sodium ion battery. *Energy. Storage. Mater.* **2024**, *71*, 103645. DOI
8. Hou, H.; Qiu, X.; Wei, W.; Zhang, Y.; Ji, X. Carbon anode materials for advanced sodium-ion batteries. *Adv. Energy. Mater.* **2017**, *7*, 1602898. DOI
9. Pan, H.; Hu, Y.; Chen, L. Room-temperature stationary sodium-ion batteries for large-scale electric energy storage. *Energy. Environ. Sci.* **2013**, *6*, 2338. DOI
10. Lu, Y.; Lu, Y.; Niu, Z.; Chen, J. Graphene-based nanomaterials for sodium-ion batteries. *Adv. Energy. Mater.* **2018**, *8*, 1702469. DOI

11. Xu, Z.; Park, J.; Yoon, G.; Kim, H.; Kang, K. Graphitic carbon materials for advanced sodium-ion batteries. *Small. Methods.* **2019**, *3*, 1800227. DOI
12. Wen, Y.; He, K.; Zhu, Y.; et al. Expanded graphite as superior anode for sodium-ion batteries. *Nat. Commun.* **2014**, *5*, 4033. DOI
13. Kang, Y.; Jung, S. C.; Choi, J. W.; Han, Y. Important role of functional groups for sodium ion intercalation in expanded graphite. *Chem. Mater.* **2015**, *27*, 5402-6. DOI
14. Tao, F.; Liu, Y.; Ren, X.; et al. Carbon nanotube-based nanomaterials for high-performance sodium-ion batteries: Recent advances and perspectives. *J. Alloys. Compd.* **2021**, *873*, 159742. DOI
15. Balogun, M.; Luo, Y.; Qiu, W.; Liu, P.; Tong, Y. A review of carbon materials and their composites with alloy metals for sodium ion battery anodes. *Carbon* **2016**, *98*, 162-78. DOI
16. Wang, Z.; Feng, X.; Bai, Y.; et al. Probing the energy storage mechanism of quasi-metallic Na in hard carbon for sodium-ion batteries. *Adv. Energy. Mater.* **2021**, *11*, 2003854. DOI
17. Nita, C.; Zhang, B.; Dentzer, J.; Matei, G. C. Hard carbon derived from coconut shells, walnut shells, and corn silk biomass waste exhibiting high capacity for Na-ion batteries. *J. Energy. Chem.* **2021**, *58*, 207-18. DOI
18. Tang, Y.; He, J.; Peng, J.; et al. Electrochemical behavior of the biomass hard carbon derived from waste corncob as a sodium-ion battery anode. *Energy. Fuels.* **2024**, *38*, 7389-98. DOI
19. Lim, G. H.; Lee, J.; Choi, J.; Kang, Y. C.; Roh, K. C. Efficient utilization of lignin residue for activated carbon in supercapacitor applications. *Mater. Chem. Phys.* **2022**, *284*, 126073. DOI
20. Zhang, W.; Qiu, X.; Wang, C.; et al. Lignin derived carbon materials: current status and future trends. *Carbon. Res.* **2022**, *1*, 14. DOI
21. Chen, C.; Sun, K.; Huang, C.; et al. Investigation on the mechanism of structural reconstruction of biochars derived from lignin and cellulose during graphitization under high temperature. *Biochar* **2023**, *5*, 229. DOI
22. Yao, M.; Bi, X.; Wang, Z.; Yu, P.; Dufresne, A.; Jiang, C. Recent advances in lignin-based carbon materials and their applications: a review. *Int. J. Biol. Macromol.* **2022**, *223*, 980-1014. DOI
23. Zhu, Y.; Yang, T. X.; Qi, B. K.; Li, H.; Zhao, Q. S.; Zhao, B. Acidic and alkaline deep eutectic solvents (DESs) pretreatment of grapevine: component analysis, characterization, lignin structural analysis, and antioxidant properties. *Int. J. Biol. Macromol.* **2023**, *236*, 123977. DOI
24. Oh, Y.; Park, S.; Jung, D.; Oh, K. K.; Lee, S. H. Effect of hydrogen bond donor on the choline chloride-based deep eutectic solvent-mediated extraction of lignin from pine wood. *Int. J. Biol. Macromol.* **2020**, *165*, 187-97. DOI
25. Ji, Q.; Tan, C. P.; Yagoub, A. E. A.; Chen, L.; Yan, D.; Zhou, C. Effects of acidic deep eutectic solvent pretreatment on sugarcane bagasse for efficient 5-hydroxymethylfurfural production. *Energy. Technol.* **2021**, *9*, 2100396. DOI
26. Tian, D.; Guo, Y.; Hu, J.; et al. Acidic deep eutectic solvents pretreatment for selective lignocellulosic biomass fractionation with enhanced cellulose reactivity. *Int. J. Biol. Macromol.* **2020**, *142*, 288-97. DOI
27. da, C. L. A. M.; João, K. G.; Rubik, D. F.; et al. Pre-treatment of lignocellulosic biomass using ionic liquids: wheat straw fractionation. *Bioresour. Technol.* **2013**, *142*, 198-208. DOI
28. Liu, Y.; He, Z.; Shankle, M.; Tewolde, H. Compositional features of cotton plant biomass fractions characterized by attenuated total reflection Fourier transform infrared spectroscopy. *Ind. Crops. Prod.* **2016**, *79*, 283-6. DOI
29. Morán-Aguilar, M. G.; Calderón-Santoyo, M.; de, S. O. R. P.; Aguilar-Uscanga, M. G.; Domínguez, J. M. Deconstructing sugarcane bagasse lignocellulose by acid-based deep eutectic solvents to enhance enzymatic digestibility. *Carbohydr. Polym.* **2022**, *298*, 120097. DOI PubMed
30. Ong, H. C.; Yu, K. L.; Chen, W.; et al. Variation of lignocellulosic biomass structure from torrefaction: a critical review. *Renew. Sustain. Energy. Rev.* **2021**, *152*, 111698. DOI
31. Kumar, S.; Sharma, S.; Arumugam, S. M.; Miglani, C.; Elumalai, S. Biphasic separation approach in the DES biomass fractionation facilitates lignin recovery for subsequent valorization to phenolics. *ACS. Sustain. Chem. Eng.* **2020**, *8*, 19140-54. DOI
32. Ji, Q.; Yu, X.; Wu, P.; et al. Pretreatment of sugarcane bagasse with deep eutectic solvents affect the structure and morphology of lignin. *Ind. Crops. Prod.* **2021**, *173*, 114108. DOI
33. Zhang, M.; Tian, R.; Tang, S.; et al. The structure and properties of lignin isolated from various lignocellulosic biomass by different treatment processes. *Int. J. Biol. Macromol.* **2023**, *243*, 125219. DOI
34. Shemet, V.; Pomytkin, A.; Neshpor, V. High-temperature oxidation behaviour of carbon materials in air. *Carbon* **1993**, *31*, 1-6. DOI
35. Terzyk, A. P. The influence of activated carbon surface chemical composition on the adsorption of acetaminophen (paracetamol) in vitro: Part II. TG, FTIR, and XPS analysis of carbons and the temperature dependence of adsorption kinetics at the neutral pH. *Colloid. Surface. A.* **2001**, *177*, 23-45. DOI
36. Han, J.; Jeong, S.; Lee, J. H.; Choi, J. W.; Lee, J.; Roh, K. C. Structural and electrochemical characteristics of activated carbon derived from lignin-rich residue. *ACS. Sustain. Chem. Eng.* **2019**, *7*, 2471-82. DOI
37. Zhang, H.; Ming, H.; Zhang, W.; Cao, G.; Yang, Y. Coupled carbonization strategy toward advanced hard carbon for high-energy sodium-ion battery. *ACS. Appl. Mater. Interfaces.* **2017**, *9*, 23766-74. DOI
38. Wang, H.; Shi, Z.; Jin, J.; Chong, C.; Wang, C. Properties and sodium insertion behavior of Phenolic Resin-based hard carbon microspheres obtained by a hydrothermal method. *J. Electroanal. Chem.* **2015**, *755*, 87-91. DOI
39. Pei, L.; Cao, H.; Yang, L.; et al. Hard carbon derived from waste tea biomass as high-performance anode material for sodium-ion batteries. *Ionics* **2020**, *26*, 5535-42. DOI
40. Zhu, X.; Jiang, X.; Liu, X.; Xiao, L.; Cao, Y. A green route to synthesize low-cost and high-performance hard carbon as promising

sodium-ion battery anodes from sorghum stalk waste. *Green. Energy. Environ.* **2017**, *2*, 310-5. DOI

41. Bai, Y.; Wang, Z.; Wu, C.; et al. Hard carbon originated from polyvinyl chloride nanofibers as high-performance anode material for Na-ion battery. *ACS. Appl. Mater. Interfaces.* **2015**, *7*, 5598-604. DOI
42. Gao, T.; Zhou, Y.; Jiang, Y.; Xue, Z.; Ding, Y. Bamboo waste derived hard carbon as high performance anode for sodium-ion batteries. *Diam. Relat. Mater.* **2024**, *150*, 111737. DOI
43. Zhong, B.; Liu, C.; Xiong, D.; et al. Biomass-derived hard carbon for sodium-ion batteries: basic research and industrial application. *ACS. Nano.* **2024**, *18*, 16468-88. DOI
44. Shen, F.; Zhu, H.; Luo, W.; et al. Chemically crushed wood cellulose fiber towards high-performance sodium-ion batteries. *ACS. Appl. Mater. Interfaces.* **2015**, *7*, 23291-6. DOI